



# A method for estimating the state of health of lithium-ion batteries based on physics-informed neural network

Jinhua Ye<sup>a,c</sup>, Quan Xie<sup>a</sup>, Mingqiang Lin<sup>b,\*</sup>, Ji Wu<sup>d</sup>

<sup>a</sup> School of Mechanical Engineering and Automation, Fuzhou University, Fuzhou, Fujian, 350116, PR China

<sup>b</sup> Quanzhou Institute of Equipment Manufacturing, Fujian Institute of Research on the Structure of Matter, Chinese Academy of Sciences, Jinjiang, Fujian, 362200, PR China

<sup>c</sup> Fujian Key Laboratory of Special Intelligent Equipment Safety Measurement and Control, Fuzhou, 350003, PR China

<sup>d</sup> School of Automotive and Transportation Engineering, Hefei University of Technology, Hefei, Anhui, 230009, PR China



## ARTICLE INFO

Handling Editor: Prof X Ou

**Keywords:**

Lithium-ion battery  
State of health  
Neural network  
Physical constraints  
Incremental capacity curves

## ABSTRACT

Data-driven methods have been widely used to estimate the State of health (SOH) of Lithium-Ion batteries (LIBs). However, these methods lack interpretability. In response to this issue, this article proposes a method called Physics-informed neural network (PIFNN) to enhance the interpretability of predictions made by a feedforward neural network (FNN). First, the features are extracted from incremental capacity (IC) curves and differential temperature curves, which can characterize battery aging from different perspectives. Specifically, the peaks of the IC curves (P-IC) reflect the electrochemical reactions that occur during the charge-discharge processes of LIBs. The decline of the P-IC is related to the loss of active materials in LIBs, which is a major cause of the decrease of the SOH. This article converts the monotonous relationship between the P-IC and the SOH into physical constraints to guide the “learning process” of the model. In the prediction process, a physics-constrained secondary “training” is applied to the FNN predictions to further enhance interpretability and improve prediction accuracy. The feasibility of the proposed method is validated using the Oxford and NASA battery datasets. The results indicate that PIFNN effectively improves prediction accuracy and reduces errors to below 1.5 %.

## 1. Introduction

In today's society, Lithium-Ion batteries (LIBs), as one of the primary energy storage systems, are experiencing an increasingly widespread application [1]. The lithium-ion battery is widely regarded as a promising device for achieving a sustainable society [2]. They possess several significant advantages, such as high energy density, high specific energy, low pollution, and low energy consumption [3]. These assets make LIBs the preferred energy storage technology for numerous modern electronic devices and clean energy solutions. However, due to their extensive applications in various complex external working environments and their complex and variable internal electrochemical properties, the degradation process of LIBs is highly intricate [4–6]. Compared to the expenses required for timely replacement or maintenance, severe LIBs' failures may lead to extremely adverse consequences and significant pecuniary losses [7]. Therefore, prognostics and health management is crucial to the reliability and safety of lithium-ion batteries [8], and the battery management system (BMS) is an indispensable core

component of battery technology [9]. It not only ensures the safety, reliability, and efficient operation of the battery, while also extending its lifespan, but it also provides data to support the optimization and maintenance of the battery system. State monitoring is a basic function of BMS [10], which includes the estimation of the State of Charge, the SOH, the State of Energy, and the State of Power. Among these states, the SOH of LIBs reflects the deterioration in performance during charge and discharge cycles and is one of the key state parameters [11]. In some cases, it may even impact the reliability and safety of electric vehicles equipped with these battery configurations. Hence, accurately estimating the SOH of LIBs is crucial within the BMS.

### 1.1. Literature review

Currently, methods that estimate the SOH of LIBs can be broadly categorized into two main types: physics-based model approaches (PBMs) and data-driven model approaches. Various methods based on models that are used to estimate the SOH of LIBs primarily rely on

\* Corresponding author.

E-mail address: [kdlmq@fjirsm.ac.cn](mailto:kdlmq@fjirsm.ac.cn) (M. Lin).

physical or mathematical models to monitor and assess the performance and lifespan of the batteries. One commonly used model to describe the physical processes of LIBs is the pseudo-two-dimensional model proposed by Doyle et al. [12]. Other models are also utilized for estimating the SOH of LIBs. For instance, Xiong et al. [13] conducted degradation analysis using electrochemical impedance spectra for different SOH levels and an online parameter identification method based on fractional-order impedance models. Pinson et al. [14] considered the growth at the solid electrolyte interface as the primary cause of LIBs' degradation. They accurately explained capacity fade phenomena using a single particle model and predicted future degradation based on limited data from accelerated aging tests. Xu et al. [15] described battery dynamics using an equivalent circuit model. They applied recursive least squares for online parameter identification, used an unscented Kalman filter to estimate battery state, and associated SOH with capacity fade caused by irreversible lithium losses. While PBMs can describe the electrochemical behavior during the degradation of LIBs, practical applications present challenges. Firstly, PBMs heavily depend on model selection, and most physical models have specific conditions. Current PBMs may not capture all physical degradation mechanisms and electrochemical behaviors during LIBs' degradation. This can lead to situations where the physical model may fail, particularly in certain specific or extreme cases. Additionally, PBMs relying on models typically have high requirements for data quality. They often require precise measurement data and are sensitive to noise during the measurement process. Despite providing reasonably accurate SOH estimates, PBMs require more complex models and computational resources, making them less ideal for practical applications.

In recent years, with the advancement of computer technology, data-driven methods for estimating the SOH are widely used [16]. Data-driven methods for monitoring the SOH of LIBs are typically achieved by analyzing historical data, including parameters such as current, voltage, capacitance, and impedance [17]. These methods only require the collection of LIBs' aging data and do not necessitate an analysis of the degradation mechanisms of LIBs [18]. As a result, data-driven approaches are becoming increasingly popular. For instance, Meng et al. [19] derived the minimum signal-to-noise ratio requirements for each frequency component of the excitation signal by analyzing the quantitative relationship between impedance deviation and sampling error. By applying a comprehensive optimization framework, they solved for the optimal amplitude and phase angle of all frequency components to form a comprehensively optimized binary sequence for extracting battery impedance response. Lin et al. [20] decomposed LIBs' capacity into a global declining trend and local fluctuations. They trained a gated recurrent unit neural network to capture the long-term global declining trend without experiencing gradient disappearance. Additionally, they used a hidden Markov model to capture local fluctuations and quantify the uncertainty caused by capacity recovery phenomena in LIBs' degradation. Meng et al. [21] applied a multi-scenario transferable learning framework with few-shot to predict the Li-ion battery lifespan trajectory. Meng et al. [22] proposed a fast impedance extraction method for electrochemical impedance spectroscopy measurement of lithium-ion batteries, which integrates the power spectrum and frequency characteristics of pseudorandom sequence excitation signals into impedance measurement. All inherent connections of impedance, frequency, and power spectrum are used to form a new fusion mechanism, which can effectively extract battery impedance through automatic selection programs. However, it is precisely because establishing data-driven models does not require understanding the aging mechanisms of LIBs, and data-driven models often involve dimensionality reduction and feature engineering [23], that the predictions of data-driven models may violate physical principles, making them unrealistic and unreasonable. This also leads to a lack of predictive interpretability for purely data-driven models.

Physics-informed machine learning (PIML) has emerged as a promising approach to address the lack of interpretability in purely data-

driven models. PIML integrates principles from physics with data-driven methods, utilizing physical knowledge to guide and enhance the performance of machine learning models [24]. This methodology has been applied in various domains. And in the context of LIBs, researchers have also explored the application of PIML. For example, Yu et al. [25] integrated the open-circuit voltage and reaction polarization resistance of a solid electrolyte membrane as critical physical information into a deep-learning model. These variables were combined with the original input to construct the physics-informed deep learning framework. Singh et al. [26] on the other hand, predicted the charging state and state health of LIBs by incorporating the partial differential equations of Fick's diffusion law from a single-particle model into the training process of a neural network.

## 1.2. Contributions

The P-IC exhibits distinct shapes, heights, and positions, which indicate the electrochemical reactions that occur during the degradation of LIBs [27]. The decrease in the P-IC is associated with the loss of active materials in LIBs [28]. With an increase in the number of charge-discharge cycles of LIBs, the active materials continuously degrade because they are unable to accommodate lithium. The degradation of active materials is one of the primary reasons for the degradation of LIBs [29,30]. Hence, it can be inferred that there is a monotonic relationship between the P-IC and the SOH of LIBs. This work aims to embed physical knowledge into data-driven models and presents an approach for estimating the SOH of LIBs using the physics-constrained neural network. By converting the monotonous relationship between the P-IC and the SOH of LIBs into physical constraints, this method aids in training the model. Moreover, during the validation of the model's performance, the model undergoes secondary "training" to promptly adjust itself, thereby enhancing model interpretability and precision. The specific contributions are as follows:

- (1) The monotonic relationship between the P-IC and SOH mentioned earlier is utilized as a physical constraint.
- (2) A physics-constrained secondary "training" is applied to the feedforward neural network (FNN) predictions to further enhance interpretability and improve prediction accuracy.
- (3) The performance of the model is validated on the Oxford and NASA datasets. The effectiveness is discussed separately for training with the physical constraint guiding the model training of PIFNN and for the secondary "training" of PIFNN.

## 2. Research methodology

As illustrated in Fig. 1, PIFNN can be divided into three processes: feature extraction, training of the neural network based on physical constraints, and secondary adjustment based on physical constraints. Firstly, we extract prominent features that describe the aging process of the battery by acquiring the IC curve and the DT curve. Subsequently, physical constraints are incorporated into the training process of the neural network model to guide its training. Finally, during the testing phase, a secondary "training" of the neural network model is conducted based on physical constraints to enhance the interpretability of predictions and improve prediction accuracy.

### 2.1. Feature acquisition

This study conducted experiments using the Oxford Battery Dataset [31,32], which includes data from eight Kokam pouch cells with a nominal capacity of 740mAh and labeled as Cell1 to Cell8. The cathode material of LIBs consists of lithium cobalt oxide and lithium nickel cobalt oxide, while the anode material is graphite. In the aging experiments, the eight LIBs were repeatedly charged at a 2C current and subjected to dynamic condition discharges to simulate real-world

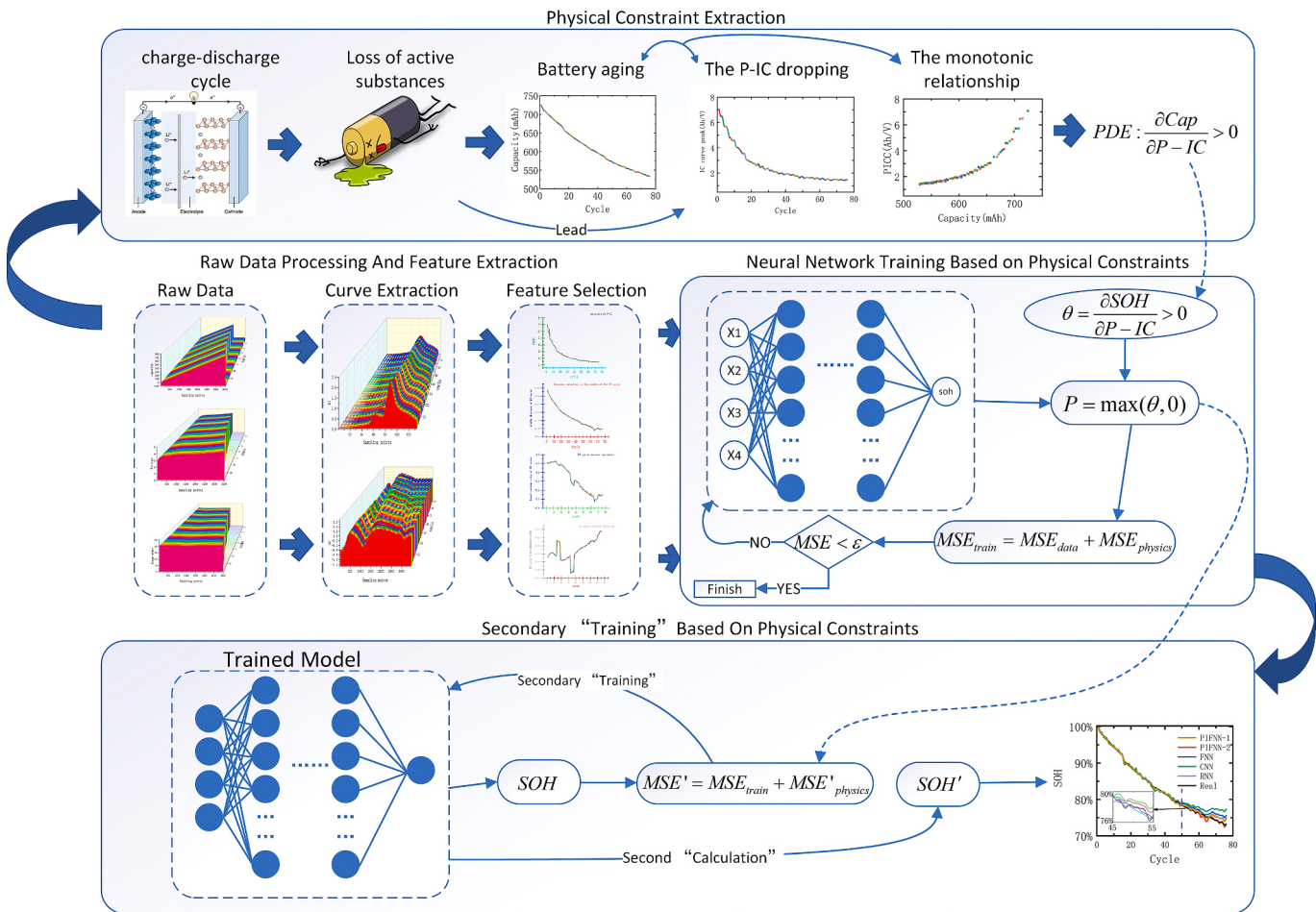


**Fig. 1.** The flowchart of the PIFNN training scheme and secondary “training”.

driving scenarios for automobiles. Every 100 aging cycles, a 1C current charge-discharge was performed to measure the capacity of LIBs. Parameters such as current, voltage, and surface temperature were recorded by the Bio-logic MPG-205 battery tester at 1-s intervals. This study defines the SOH as the ratio of the maximum capacity  $Q$  of each cycle to the rated capacity  $Q_0$ :

$$SOH = \frac{Q}{Q_0} \quad (1)$$

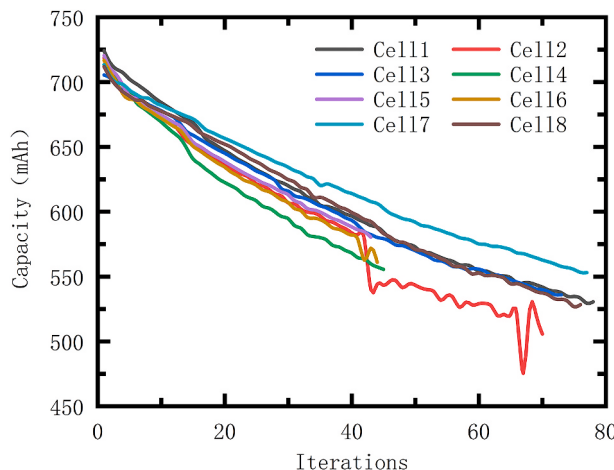


**Fig. 2.** Oxford battery dataset capacity degradation.

**Fig. 2** depicts the decrease in capacity with the number of cycles in the Oxford Battery Dataset.

The IC curve of LIBs includes many features that reflect the aging process and can further reveal the aging mechanism. For instance, Lin et al. [33] sampled voltage curves and used incremental capacity to identify peak features in the IC curve, which describes the aging process of LIBs. Signals such as LIBs’ surface temperature and force can characterize LIBs aging from various perspectives.

In particular, the temperature signal is one of the crucial parameters for BMS. Tian et al. [34] analyzed temperature difference curves during constant charging and found a strong correlation with the SOH. They used support vector regression to establish the relationship between the temperature and the SOH. Therefore, this study chooses to extract IC curves and DT curves and select features from them for the SOH estimation. The methods for obtaining IC curves and DT curves are as follows:

**IC Curve Acquisition:** The IC curve refers to the curve depicting the variation of current with voltage during the charging and discharging processes of a battery. It is obtained by comparing the incremental capacity during the constant current charging phase with the corresponding voltage changes. Therefore, in the constant current charging mode, the mathematical formula for the IC curve can be expressed as follows:

$$IC = \frac{dQ}{dU} = I \cdot \frac{dt}{dU} \quad (2)$$

where  $Q$  represents capacity,  $U$  represents voltage,  $I$  represents current, and  $t$  represents sampling time.

To mitigate the impact of noise, this article uses the finite difference method to obtain the IC curve. The calculation formula is as follows:

$$\frac{dQ}{dU} \approx \frac{\Delta Q}{\Delta U} = \frac{Q_k - Q_{k-1}}{U_k - U_{k-1}} \quad (3)$$

where  $Q_k$  and  $Q_{k-1}$  represent the battery capacity charged at time steps k and k-1, respectively, while  $U_k$  and  $U_{k-1}$  denote the battery terminal voltage at time steps k and k-1, respectively. Furthermore, we apply Gaussian filtering to smooth the obtained IC curve and reduce the influence of noise.

The analysis of IC curves is considered to be one of the key technologies for studying LIBs aging mechanisms because it provides valuable information about LIBs' performance and status, which aids in a deeper understanding of the LIBs' aging process. LIBs aging is the gradual decline in LIBs' performance, typically caused by various factors such as material degradation, electrolyte loss, and changes in electrode films over time. These aging processes leave traces in the IC curves, such as voltage drops and increased internal resistance. By observing these traces, it is possible to effectively identify the extent of LIBs aging. The analysis of the IC curve focuses on the electrode level of the LIBs. One significant advantage of this method is that it can convert the plateau of LIBs' voltage into distinct P-IC. These peaks can effectively describe the processes of inserting and extracting lithium-ion active materials, thereby revealing the phase-change characteristics within LIBs. Hence, the analysis of the IC curve is considered a crucial technique for studying LIBs' aging mechanisms.

This article uses the IC curves obtained from the Cell 1 dataset in the Oxford dataset as an example to observe the changes in IC curves during the LIBs' charge-discharge cycles. By examining Fig. 3, it can be observed that as LIBs degrade, the overall IC curve becomes smoother, and the P-IC gradually decreases.

The decline in the peak of the IC curve is closely associated with the loss of active materials within LIBs. As the number of charge-discharge cycles increases, the active materials continuously deteriorate due to their inability to effectively incorporate lithium. Specifically, the loss of active materials of LIBs is one of the primary causes of battery degradation. Based on this, as depicted in Fig. 4, there is a monotonic relationship between the P-IC and the SOH of LIBs.

Finally, obtaining the P-IC does not require using the full charge/discharge cycle and only the segment of charge-discharge data containing the P-IC is needed. Therefore, the P-IC can serve as an effective characteristic for describing capacity degradation. Moreover, there is a monotonic relationship between the P-IC and the SOH of LIBs.

**Temperature Change Curve Acquisition:** Due to the limited ability of the sensors used to measure temperature, direct calculations are

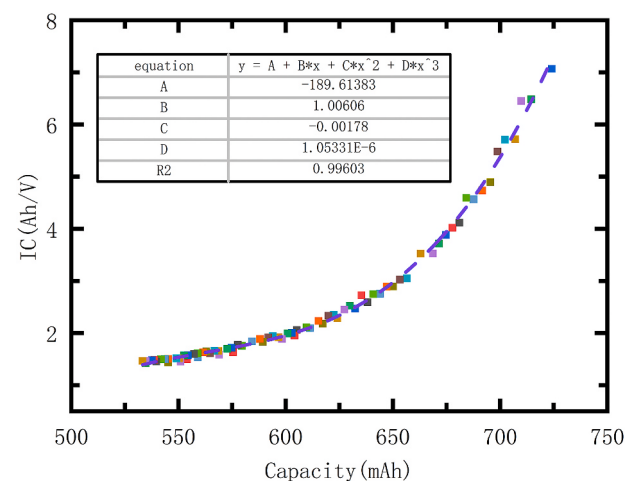


Fig. 4. The relationship between the P-IC and capacity.

susceptible to external noise, resulting in significant deviations. To mitigate the impact of noise, this article uses the finite difference method to obtain the DT curve. The calculation formula is as follows:

$$DT(k) \approx \frac{T(k+L) - T(k)}{L} \quad (4)$$

where  $T$  represents the temperature, and  $L$  represents the sampling interval. The selection of the sampling interval,  $L$ , has a significant impact on obtaining the DT curve. Choosing a value that is too large can result in the loss of inherent characteristics of the DT curve, while choosing a value that is too small may lead to significant interference from external noise on the DT curve. Therefore, selecting an appropriate sampling interval is crucial. In this study, we set the sampling interval as  $L = 40$ . Additionally, we applied Gaussian filtering to smooth the obtained DT curve and reduce the impact of noise.

Taking a portion of the DT curve extracted from the Cell 1 dataset as an example, we observe the corresponding changes in the DT curve with battery degradation. As depicted in Fig. 5, it is evident that the temperature transition rate in the LIBs is strongly correlated with the SOH. The temperature transition rate gradually decreases with the use of LIBs, and then it gradually increases. As LIBs undergo gradual degradation, the left peak of the DT curve gradually decreases, the overall value of the middle valley increases, and the voltage difference between them gradually narrows. In summary, various sections of the battery temperature change curve, such as the left peak, the middle valley, and the voltage difference between them, demonstrate specific patterns as the

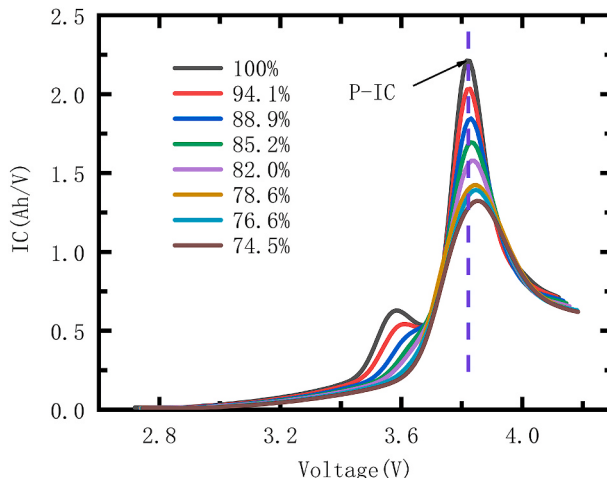


Fig. 3. The change of IC curves with the deterioration of the battery.

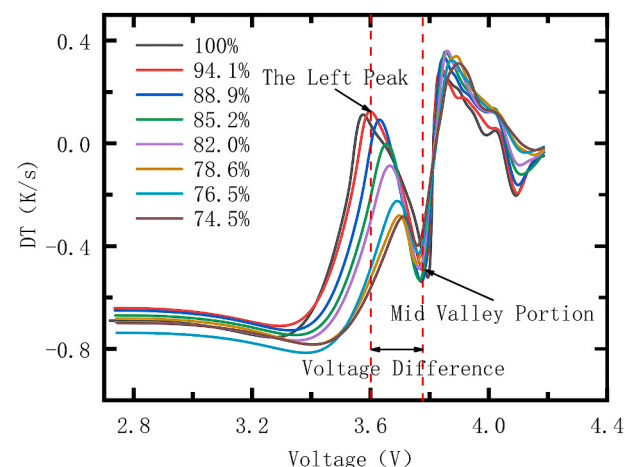


Fig. 5. The temperature change curve in response to battery degradation.

SOH decreases. These regularities can be used to describe the decline in LIBs' capacity. Therefore, the left peak, middle valley, and voltage difference between them in the DT curve can be effective features for describing the degradation of LIBs.

In conclusion, this study identifies four features that reflect the degradation in the SOH of LIBs. These features include the left peak, the middle valley, and the voltage difference between them in the DT curve, as well as the P-IC.

## 2.2. Neural networks with physical constraints

In this study, we utilize FNN to estimate and predict the SOH of LIBs. The network consists of three types of neural network layers: the hidden layer, the input layer, and the output layer. It processes input data through the network and computes the final output in a process known as forward propagation. This is a fundamental computational process in neural networks and serves as the foundation for inference or prediction. The forward propagation process begins with the input layer. The input layer receives raw input data, such as the four features of the LIBs mentioned previously. Each input feature corresponds to a neural unit in the input layer. During forward propagation, each neural unit is connected to every neural unit in the preceding layer. Each connection has a weight and a bias. The weight signifies the strength of the connection, while the bias represents the activation threshold of the neural unit. For each neural unit, a weighted sum is calculated. This process involves multiplying the output from the previous layer by the corresponding weight and then summing up these products. Afterward, the bias is added. This results in a weighted sum. The formula is as follows:

$$z(x) = \alpha(Wx + b) \quad (5)$$

where  $x$  represents the output of the neurons from the previous layer,  $\alpha$  represents the selected non-linear parameter called the activation function,  $W$  corresponds to the weights associated with the connections between neurons, and  $b$  denotes the bias term used for correction. Subsequently, the final output of the neuron is computed by applying the activation function which enables the model to acquire non-linear properties, enabling the neural network to model non-linear relationships. Ultimately, forward propagation applies these computations to all neurons in each layer, passing through them layer by layer until they reach the output layer which generates the final predictions. Once the input data passes through each layer of the network, the forward propagation process is completed. The final output is then used to calculate the loss function, which evaluates the model's performance during training.

The backpropagation algorithm operates by calculating the gradients of the loss function in relation to every weight and bias in the network. It starts from the output layer and moves backward through each layer. Before the backpropagation algorithm starts, the forward propagation is executed first. After completing the forward propagation, to calculate the discrepancy between the model's predictions and the actual labels to assess the network's performance, the loss function is used. Subsequently, the gradients of each parameter are calculated using the chain rule. Once the gradients for each parameter are computed, gradient descent or its variants can be used to update these parameters. Gradient descent updates the weights and biases in the opposite direction of the gradient to minimize the loss function. The steps involving forward propagation, loss computation, backpropagation, and parameter updates are repeated until the loss function converges or reaches pre-defined stopping conditions.

To enhance the interpretability of fully connected neural networks, this paper incorporates physical knowledge by translating it into constraint conditions that guide the neural network model. As mentioned earlier, the P-IC exhibits a monotonic relationship with the SOH of LIBs. We incorporate this physical information as a constraint into the loss function of the neural network to guide its training.

Typically, the loss function of a conventional neural network is defined as the mean squared error:

$$\text{loss}_{\text{data}} = \frac{1}{2} \sum_{i=1}^N e_i^2 = \frac{1}{2} \sum_{i=1}^N (f(x^i, W, M) - SOH_i)^2 \quad (6)$$

where  $N$  represents the number of training samples,  $W$  denotes the network parameter vector,  $M$  represents the network model,  $f$  is the network output function, and  $SOH_i$  represents the true value of the SOH. We can incorporate physical constraints into the loss function using the following formula:

$$\theta(x^i) = \frac{\partial \hat{f}(x^i, W, M)}{\partial x_1^i} > 0 \quad (7)$$

where  $x_1^i$  represents the P-IC,  $\hat{f}$  represents the prediction of neural networks,  $\theta(x^i)$  represents the physical constraint learned from the P-IC.

According to the optimization method of the loss function, we can obtain the optimal solution to the constrained optimization problem illustrated in equation (6) by constructing the following loss function:

$$\text{loss}_{\text{physics}} = \sum_{i=1}^N [\min(0, \theta(x^i))]^2 \quad (8)$$

The final introduction of the loss function with physical constraint can be expressed as follows:

$$\min \text{loss}_{\text{train}} = \min (\text{loss}_{\text{data}} + \omega_1 \text{loss}_{\text{physics}}) \quad (9)$$

## 2.3. Online adjustment in the testing process

Even though the neural network, after training, has improved its generalization by adhering to the physical limitation of the training set, it may still make predictions during testing that violate these constraints. Therefore, we choose to incorporate a secondary "training" phase during the testing process. This involves an online identification and adjustment to better align the predicted values with the physical equations. This improves the interpretability of the neural network and improves the accuracy of the model's predictions. The specific method involves:

- (1) Obtaining predictions from the well-trained neural network on the testing dataset and acquiring the physical loss formula for these predictions are as follows:

$$\left\{ \begin{array}{l} \text{loss}'_{\text{physics}} = \sum_{i=1}^N [\min(0, \hat{\theta}(x^i))]^2 \\ \hat{\theta}(x^i) = \frac{\partial \hat{f}(x^i, W, M)}{\partial x_1^i} > 0 \end{array} \right. \quad (10)$$

where  $\hat{\theta}(x^i)$  represents a physical constraint learned from the P-IC on the test set. And  $\text{loss}'_{\text{physics}}$  represents the physical loss obtained from physical constraint.

- (2) During testing, the second "training" is performed according to the obtained physical loss. In the second "training", the loss function consists of two parts: one part is composed of the difference between PIFNN's predictions and the ground truth values on the training set, as well as the loss incurred from violating physical constraints; the other part is composed of the loss incurred from violating physical constraints in PIFNN's predictions during testing. The formula for the loss function is as follows:

$$\left\{ \begin{array}{l} loss_{train} = loss_{train} + loss_{test} \\ loss_{train} = loss_{data} + \omega_1 loss_{physics} \\ loss_{test} = \omega_2 loss_{physics} \end{array} \right. \quad (11)$$

where  $loss_{physics}$  represents the loss incurred by PIFNN from violating physical constraints in its predictions on the training set while  $loss'_{physics}$  represents the loss incurred by PIFNN from violating physical constraints in its predictions during testing. Why to do so is to ensure that the model's predicted values in the test set adhere better to the laws of physics without losing the "knowledge" acquired during the previous training process. This allows for a second round of training. By doing so, the neural network retains the "knowledge" it acquired during the training set, while also improving the accuracy of predicted values in the test set according to the physical equations. This approach enhances the interpretability of the neural network's predictions in the test set, thereby ultimately improving prediction accuracy.

### 3. Experiments and analysis

To validate the accuracy and generality of PIFNN, we compared our method with the recurrent neural network (RNN), the convolutional neural network (CNN), and FNN. This comparison was based on the Oxford and NASA battery datasets. To scientifically describe the experimental results, this paper employs two metrics: the mean absolute error (MAE) and the root mean square error (RMSE), to compare the predictive performance of several models. The formulas for calculating both are as follows:

$$\left\{ \begin{array}{l} MAE = \frac{1}{m} \sum_{i=1}^m |y_i^* - y_i| \\ RMSE = \sqrt{\frac{1}{m} \sum_{i=1}^m (y_i^* - y_i)^2} \end{array} \right. \quad (12)$$

#### 3.1. Validation of the oxford battery dataset

This section discusses the experimental results of eight LIBs in the Oxford Battery Dataset. The approach involves using the first 60 % of each LIB's dataset as the training set and the remaining as the test set. During the training process of the model, physical constraints are introduced to aid in the training process. Subsequently, a second "training" is conducted during the validation process to adjust the model. Finally, the performance of PIFNN is re-evaluated. In these experiments, the model is configured with three hidden layers, each containing eight neurons. The weights for the physical losses,  $\omega_1$ , and  $\omega_2$ , are both set to 0.01. The learning rate is set to 0.001, and the Adam optimizer is used. The comparison results are illustrated in Figs. 6 and 7.

To validate the effectiveness of the second step of PIFNN, which involves incorporating physical constraints during training, and the third step of "retraining," this paper introduces two versions of PIFNN. The version without the third step of "retraining" is named PIFNN-1, while the version with the third step is named PIFNN-2. To facilitate comparison, the total number of iterations is fixed at 2000 for FNN, PIFNN-1, and PIFNN-2. Both PIFNN-1 and PIFNN-2 undergo a total of 2000 iterations. However, due to the two-step training process in PIFNN-2, the first training phase consists of 1600 iterations, and the second training phase consists of 400 iterations, as illustrated in Fig. 8. In Fig. 8, the left panel depicts the loss values obtained by PIFNN in two training sessions, representing the difference between predictions and ground truth on the training set, i.e., the  $loss_{data}$  in formula 9 and the  $loss_{data}$  in formula 11. Meanwhile, the right panel illustrates the loss values incurred by PIFNN from violating physical constraints in the two training sessions. In the first training session, this corresponds to the physical loss in PIFNN's predictions on the training set. In the second

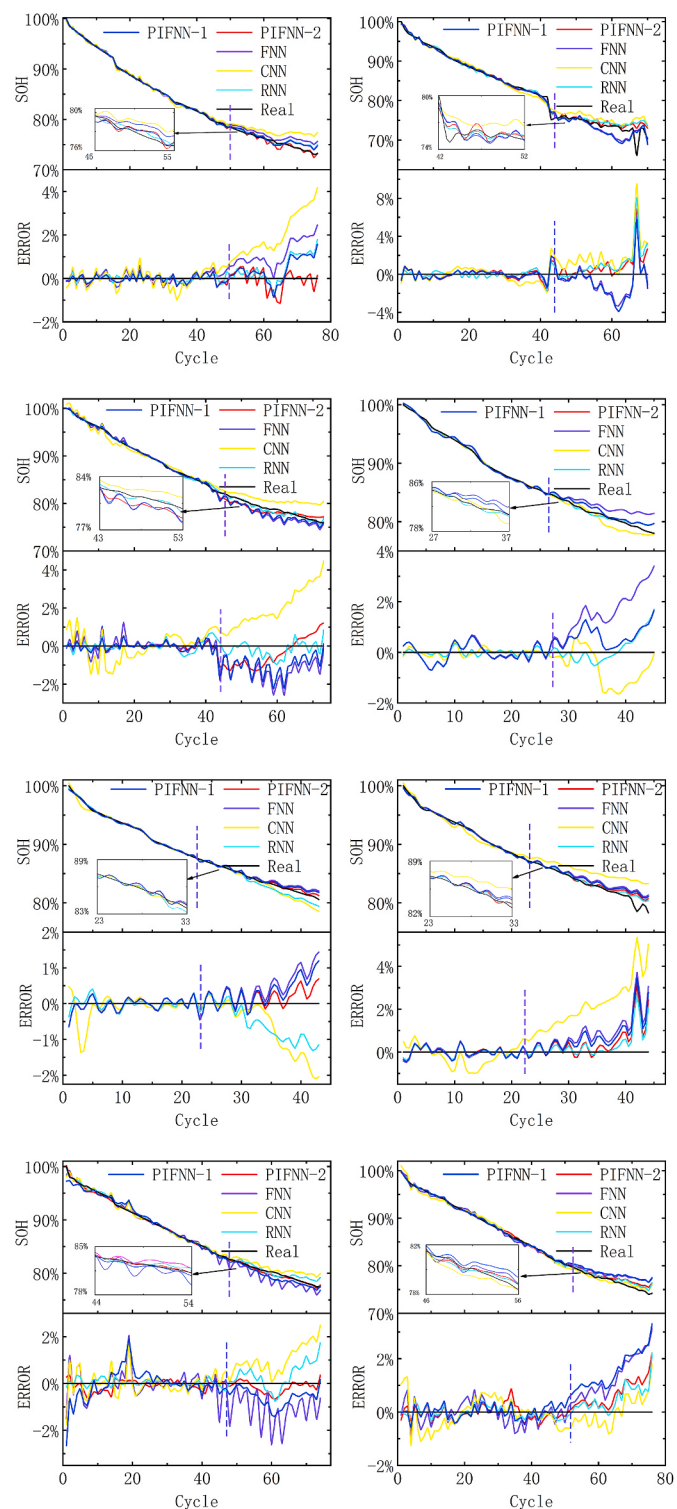


**Fig. 6.** The performance of PIFNN on the Oxford battery dataset.

training session, it encompasses the physical loss in PIFNN's predictions on both the training and testing sets. Upon observing Fig. 8, it becomes apparent that the descent curves of PIFNN-1 and PIFNN-2 are identical in the first 1600 iterations. This is because PIFNN-2 has not undergone the second training phase during this period. When compared to FNN, both PIFNN variants exhibit a more rapid decrease in the physical loss, and their corresponding ground truth errors also decrease more rapidly in the initial stages. This indicates that including physical constraint loss provides effective guidance during training. However, it is noteworthy

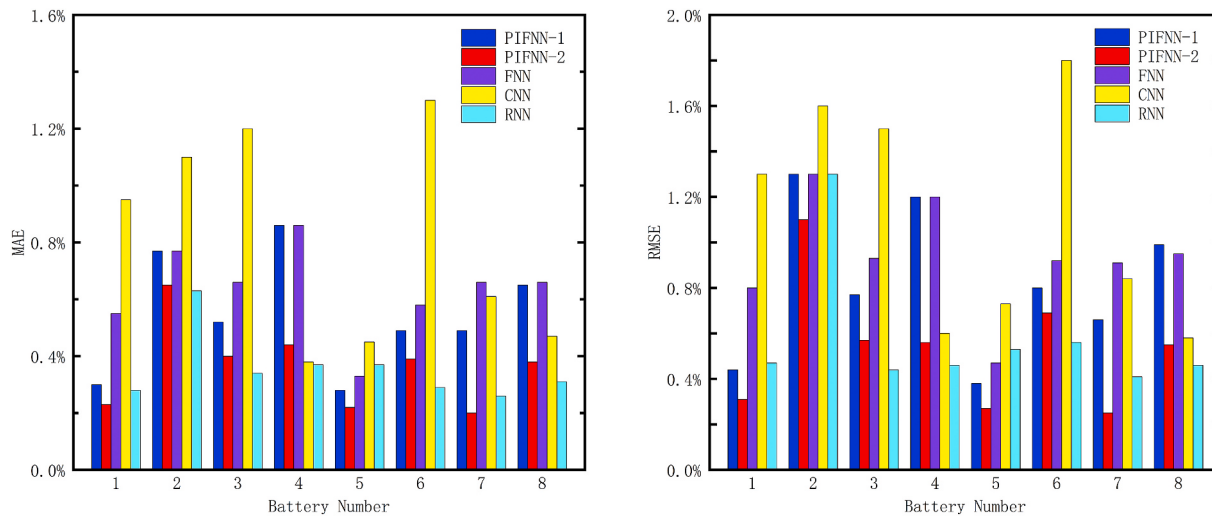


Fig. 7. Prediction errors of various models on the Oxford dataset.

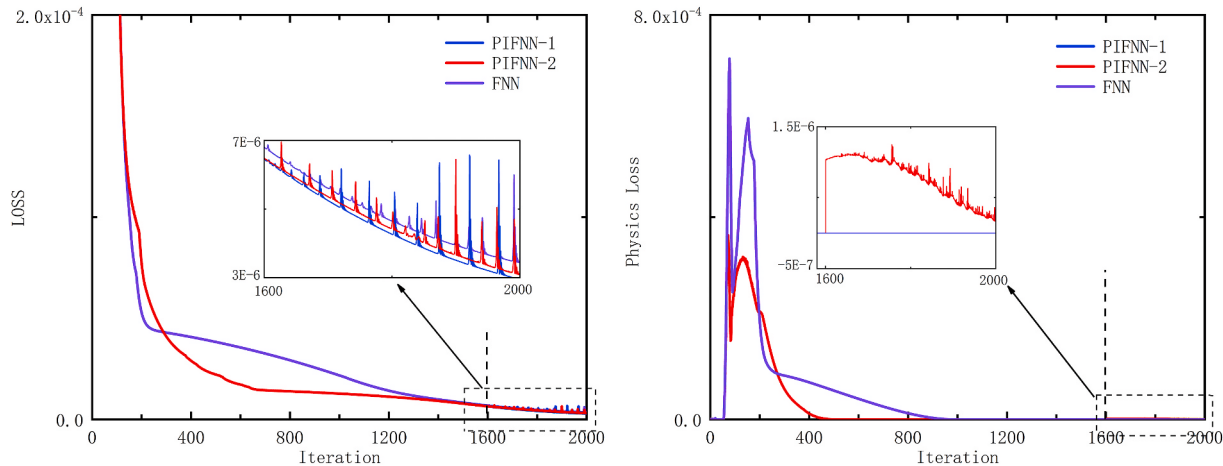


Fig. 8. Truth loss and physical loss decrease graphs of PIFNN and FNN on the Oxford dataset.

that the final physical loss of FNN also converges to zero. Moreover, the ground truth errors of all three models converge to nearly the same values in the end. The convergence patterns are influenced by the characteristics of the Oxford battery dataset. Each dataset of LIBs has a relatively small number of sampling points. The descent curves are regular, enabling FNN to achieve high training accuracy. As illustrated in Fig. 6, the performance of all models on the training set is relatively good. The physical constraint formula in this paper is represented by formula 8. However, due to the presence of noise and other factors, the P-IC and the SOH do not strictly follow a monotonic relationship. Therefore, it is not feasible to directly incorporate the physical constraints into the model using formula 8. Instead, a differential method is adopted, and the physical constraints are introduced into the model using formula 13 as follows:

$$\theta(x^i) \equiv \frac{\widehat{f}(x^i, W, M) - \widehat{f}(x^i + \Delta x, W, M)}{\Delta x} \geq 0 \quad (13)$$

where  $\Delta x$  represents the sampling interval which needs to be manually adjusted. Therefore, as shown in Fig. 8, the physical loss of the FNN becomes 0 after increasing the number of iterations. However, at 1600 iterations, PIFNN-2 undergoes a secondary “training,” and observing the small graph in Fig. 8 reveals a sudden change in its physical loss. This occurs because the secondary “training” introduces a loss associated with the model’s predicted values that violate physical constraints. As

the number of iterations increases, the physical constraint loss gradually decreases. This indicates that the third step of the secondary “training” in PIFNN-2 optimizes the model and enhances its predictive interpretability. Upon completing the entire training process, as depicted in Figs. 6 and 7, it is evident that PIFNN-1 closely aligns with FNN in terms of accuracy, as indicated by the changes shown in Fig. 8. Towards the end, the loss of physical constraints in FNN also diminishes to 0, suggesting that incorporating physical constraints during training has minimal impact.

Moreover, the predictive performance of PIFNN-2 surpasses that of PIFNN-1 and FNN. The absolute error values are nearly the same, which validates the effectiveness of the third step of the secondary “training” in PIFNN. This confirms that during this process, the model not only retains previously learned knowledge but also achieves higher accuracy during validation.

Comparing RNN and CNN, it is evident that the overall prediction performance of the CNN model is poor. This is primarily due to the fact that the CNN model used in this study is not well-suited for this experiment. However, the performance of RNN is relatively good. In fact, in some batteries, RNN’s predictive accuracy exceeds that of PIFNN. RNN’s inherent structure is suitable for time-series prediction, hence its anticipated strong predictive performance. Nevertheless, because RNN predictions lack guidance from physical “knowledge,” they can also exhibit behaviors that violate physical constraints. Additionally, the

network structure of RNN is significantly more complex than that of FNN and PIFNN, which results in lower computational efficiency and a higher vulnerability to overfitting.

### 3.2. Validation on the NASA battery dataset

To validate the generality and effectiveness of PIFNN's second step, the NASA battery dataset [35] is used to verify the performance of PIFNN. This dataset includes degradation data from three 18650 batteries, labeled as B0005, B0006, and B0007. The positive electrode material is nickel-cobalt-aluminum while the negative electrode material is graphite, and the nominal capacity of the batteries is 2 Ah. In charge-discharge cycle experiments, these three batteries were repetitively charged in constant current-constant voltage mode from 1.5 A to 4.2 V, with a cutoff current of 20 mA. Subsequently, a 2A current was applied to discharge the batteries to 2.7, 2.5, and 2.2 V, respectively. The batteries were then kept at room temperature (24 °C), and Arbin tester was used to sample current, voltage, and surface temperature. Figs. 9 and 10 depict the performance of PIFNN in the NASA battery dataset. And the meanings represented by the left and right figures in Fig. 11 are the same as those in Fig. 8. We denote iterations with and without the third step as PIFNN-1 and PIFNN-2, respectively, with a total of 3000 iterations. For PIFNN-2, the first 2500 iterations were considered as the first training phase, and the subsequent 500 iterations as the second training phase.

Firstly, observe Fig. 11. In the NASA dataset, there are no instances of physical loss values being zero. Moreover, PIFNN exhibits higher accuracy during training compared to FNN. This can be attributed to the more sampled data in the NASA dataset and the presence of abrupt changes in its SOH degradation curve. Continuing the observation of Fig. 11, it is evident that throughout the training process, the rate of decline in physical loss values for PIFNN is higher than that of FNN after incorporating physical constraints. The true value error also decreases faster for PIFNN. Figs. 9 and 10 further demonstrate that the accuracy of PIFNN-1 is higher than that of FNN, indicating the effectiveness of the second step of PIFNN for more complex battery datasets. Similarly, comparing PIFNN-1 and PIFNN-2 reveals almost identical accuracy and rates of reduction in physical loss. This similarity is due to the limited constraint capability of the physical constraints that were introduced. When the model's accuracy in training and prediction is already high, and the loss values that violate physical constraints are small, the

potential for further improvement in the model is limited. This is particularly noticeable in PIFNN-2, which exhibits suboptimal performance similar to that observed in the Oxford battery dataset. The physical constraint that has been introduced has limited restraining power, and the weight assigned to physical loss values is small, which emphasizes the need for fine-tuning the model.

When comparing the performance of PIFNN with traditional neural networks like RNN and CNN, both of them demonstrate good predictive capabilities on the NASA battery dataset. However, PIFNN's interpretability surpasses both.

## 4. Conclusion

This paper proposes a new physics-constrained SOH estimation method. Firstly, features are extracted from the IC curve and temperature change curve during the charging process of LIBs. Then, the monotonic relationship between the peak feature obtained from the IC curve and SOH is utilized as a constraint to enhance FNN training conditions. During prediction, a second "training" is performed to reduce the violation of physical constraints in the test set by the purely data-driven FNN. This process enhances the interpretability and accuracy of the FNN. To validate the feasibility of the proposed method, experiments were conducted on the Oxford and NASA battery datasets. In the experiment, the article explored the differences between PIFNN with and without secondary 'training', as well as the differences between PIFNN and FNN. The results indicate that when the prediction of FNN on the training set violates physical constraints severely, the improvement in prediction accuracy of PIFNN, guided by incorporating physical information, becomes better. Similarly, when PIFNN without secondary 'training' exhibits severe violations of physical constraints during testing, the improvement in prediction accuracy of PIFNN with secondary 'training' becomes better.

## CRediT authorship contribution statement

**Jinhua Ye:** Writing – original draft, Methodology. **Quan Xie:** Methodology, Data curation. **Mingqiang Lin:** Writing – review & editing, Validation, Formal analysis. **Ji Wu:** Visualization, Validation.

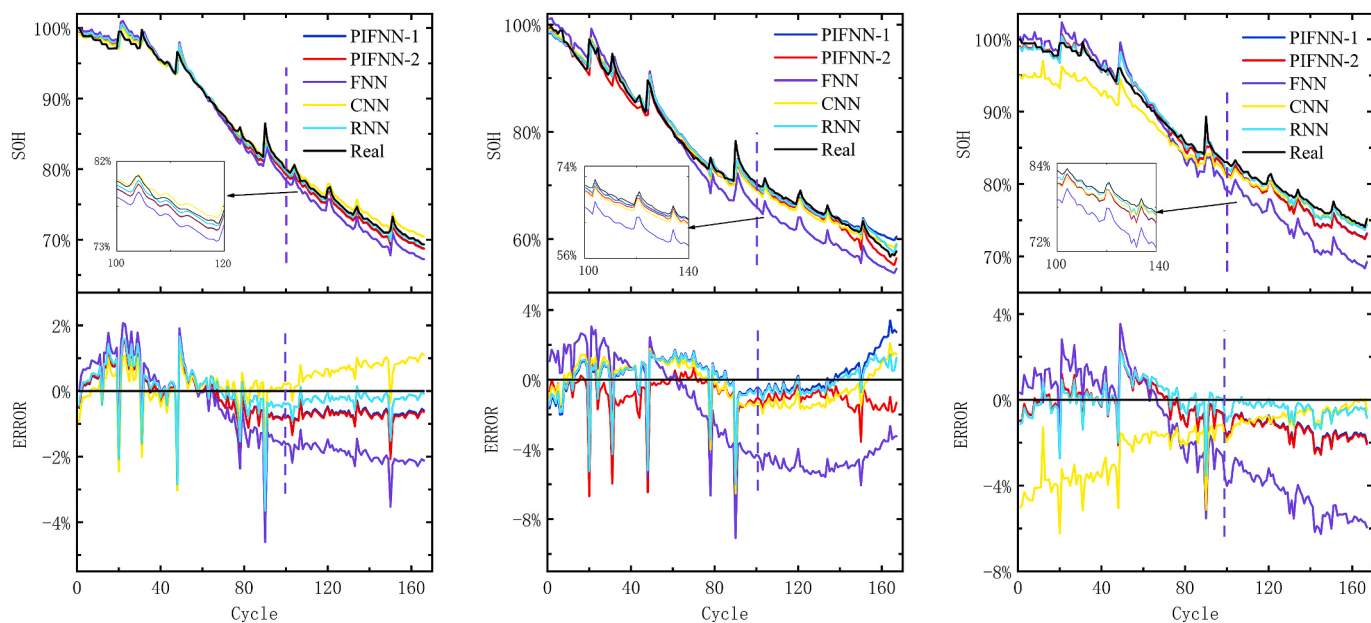


**Fig. 9.** Prediction performance of various models on the NASA dataset.

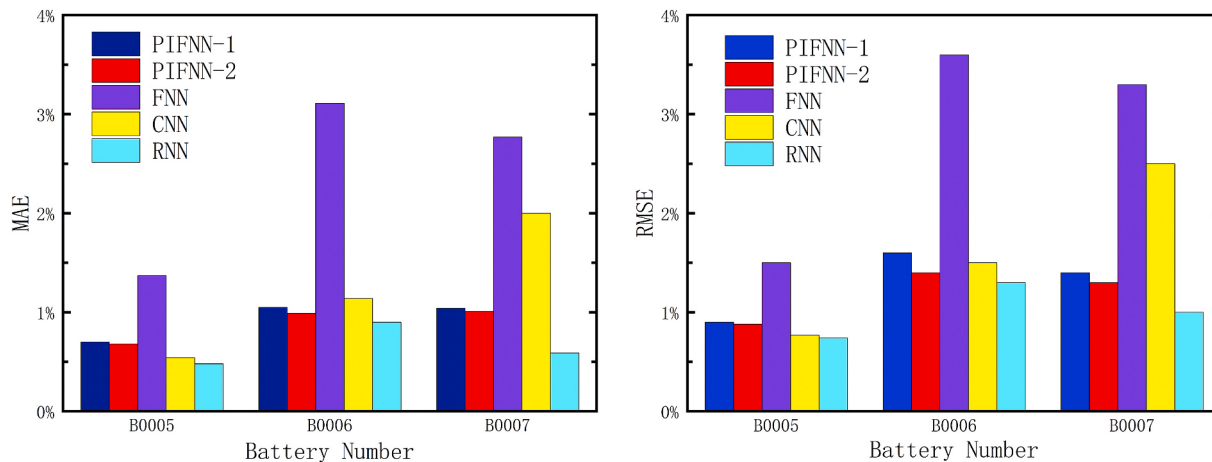


Fig. 10. Error of each model on the NASA dataset.

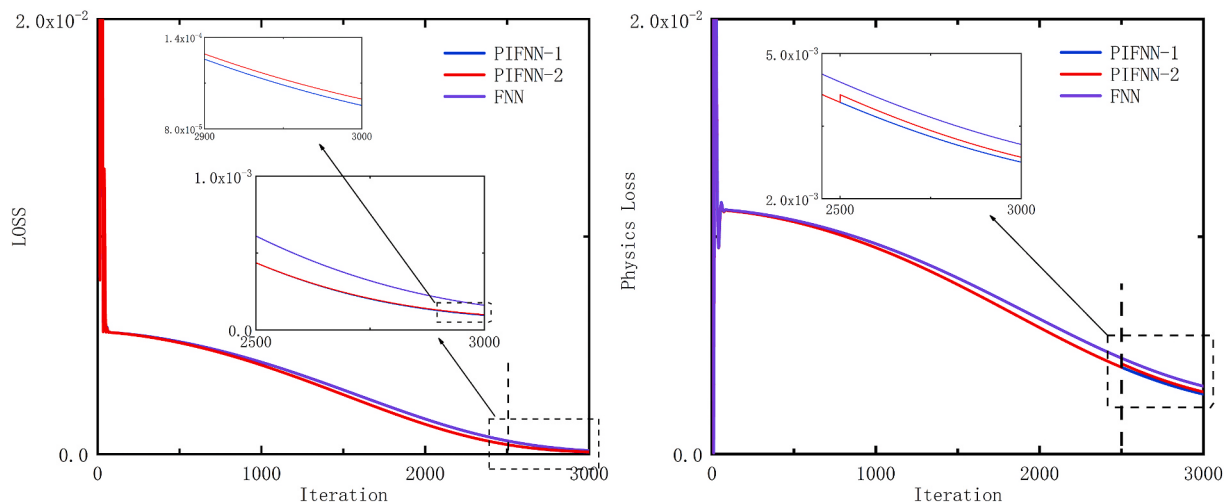


Fig. 11. PIFNN and FNN's truth loss and physical loss reduction graph on the NASA dataset.

## Declaration of competing interest

The authors declare that they have no known competing financial interests or personal relationships that could have appeared to influence the work reported in this paper.

## Data availability

Data will be made available on request.

## Acknowledgment

This work is supported in part by the Fujian Provincial Natural Science Foundation (No. 2022J01504), and in part by the Open Project Program of Fujian Key Laboratory of Special Intelligent Equipment Measurement and Control (FJIES2023KF05).

## References

- [1] Kohtz S, Xu Y, Zheng Z, Wang P. Physics-informed machine learning model for battery state of health prognostics using partial charging segments. *Mech Syst Signal Process* 2022;172:109002.
- [2] Tang X, Lai X, Zou C, Zhou Y, Zhu J, Zheng Y, Gao F. Detecting abnormality of battery lifetime from first-cycle data using few-shot learning. *Adv Sci* 2023; 2305315.
- [3] Wang S, Bai D, Fan Y, Shi H, Fernandez C. A critical review of improved deep learning methods for the remaining useful life prediction of lithium-ion batteries. *Energy Rep* 2021;7:5562–74.
- [4] Cheng KWE, Divakar BP, Wu H, Ding K, Ho HF. Battery-management system (BMS) and SOC development for electrical vehicles. *IEEE Trans Veh Technol* 2010;60(1): 76–88.
- [5] Wu J, Zhang C, Chen Z. An online method for lithium-ion battery remaining useful life estimation using importance sampling and neural networks. *Appl Energy* 2016; 173:134–40.
- [6] Dai H, Zhao G, Lin M, Wu J, Zheng G. A novel estimation method for the state of health of lithium-ion battery using prior knowledge-based neural network and Markov chain. *IEEE Trans Ind Electron* 2018;66(10):7706–16.
- [7] Xu Z, Guo Y, Saleh JH. A physics-informed dynamic deep autoencoder for accurate state-of-health prediction of lithium-ion battery. *Neural Comput Appl* 2022;34(18): 15997–6017.
- [8] Meng Huixing, et al. A hybrid method for prognostics of lithium-ion batteries capacity considering regeneration phenomena. *Energy* 2022;261:125278.
- [9] Wang Y, Zhang C, Chen Z. On-line battery state-of-charge estimation based on an integrated estimator. *Appl Energy* 2017;185:2026–32.
- [10] Lai X, Yuan M, Tang X, Zheng Y, Zhu J, Sun Y, Gao F. State-of-power estimation for lithium-ion batteries based on a frequency-dependent integer-order model. *J Power Sources* 2024;594:234000.
- [11] Yang S, Zhang C, Jiang J, Zhang W, Zhang L, Wang Y. Review on state-of-health of lithium-ion batteries: characterizations, estimations and applications. *J Clean Prod* 2021;314:128015.
- [12] Doyle M, Fuller TF, Newman J. Modeling of galvanostatic charge and discharge of the lithium/polymer/insertion cell. *J Electrochim Soc* 1993;140(6):1526.
- [13] \*\*ong R, Tian J, Mu H, Wang C. A systematic model-based degradation behavior recognition and health monitoring method for lithium-ion batteries. *Appl Energy* 2017;207:372–83.
- [14] Pinson MB, Bazant MZ. Theory of SEI formation in rechargeable batteries: capacity fade, accelerated aging and lifetime prediction. *J Electrochim Soc* 2012;160(2): A243.

- [15] Xu Z, Wang J, Lund PD, Zhang Y. Co-estimating the state of charge and health of lithium batteries through combining a minimalist electrochemical model and an equivalent circuit model. *Energy* 2022;240:122815.
- [16] Li Y, Liu K, Foley AM, Zülke A, Berecibar M, Nanini-Maury E, Hoster HE. Data-driven health estimation and lifetime prediction of lithium-ion batteries: a review. *Renew Sustain Energy Rev* 2019;113:109254.
- [17] Vichard L, Ravey A, Venet P, Harel F, Pelissier S, Hissel D. A method to estimate battery SOH indicators based on vehicle operating data only. *Energy* 2021;225:120235.
- [18] Zhang C, Luo L, Yang Z, Zhao S, He Y, Wang X, Wang H. Battery SOH estimation method based on gradual decreasing current, double correlation analysis and GRU. *Green Energy Intel Transport* 2023;2(5):100108.
- [19] Meng J, Du X, Peng J, Lin M, Song Z. Rapid lithium-ion battery impedance measurements using binary sequence with optimized frequency components. *IEEE Trans Ind Electron* 2023. <https://doi.org/10.1109/TIE.2023.3306426>.
- [20] Lin M, You Y, Wang W, Wu J. Battery health prognosis with gated recurrent unit neural networks and hidden Markov model considering uncertainty quantification. *Reliab Eng Syst Saf* 2023;230:108978.
- [21] Meng J, You Y, Lin M, Wu J, Song Z. Multi-scenarios transferable learning framework with few-shot for early lithium-ion battery lifespan trajectory prediction. *Energy* 2024;286:129682.
- [22] Meng J, Peng J, Cai L, Song Z. Rapid impedance extraction for lithium-ion battery by integrating power spectrum and frequency property. *IEEE Trans Ind Electron* 2023. <https://doi.org/10.1109/TIE.2023.3301515>.
- [23] Severson KA, Attia PM, N Perkins N, Jiang B, Yang Z, Braatz RD. Data-driven prediction of battery cycle life before capacity degradation. *Nat Energy* 2019;4(5):383–91.
- [24] Kohtz S, Xu Y, Zheng Z, Wang P. Physics-informed machine learning model for battery state of health prognostics using partial charging segments. *Mech Syst Signal Process* 2022;172:109002.
- [25] Yu H, Zhang Z, Yang K, Zhang L, Wang W, Yang S, Liu X. Physics-informed ensemble deep learning framework for improving state of charge estimation of lithium-ion batteries. *J Energy Storage* 2023;73:108915.
- [26] Singh S, Ebongue YE, Rezaei S, Birke KP. Hybrid modeling of lithium-ion battery: physics-informed neural network for battery state estimation. *Batteries* 2023;9(6):301.
- [27] Anseán D, García VM, González M, Blanco-Viejo C, Viera JC, Pulido YF, Sánchez L. Lithium-ion battery degradation indicators via incremental capacity analysis. *IEEE Trans Ind Appl* 2019;55(3):2992–3002.
- [28] Birk C, Roberts MR, McTurk E, Bruce PG, Howey DA. Degradation diagnostics for lithium ion cells. *J Power Sources* 2017;341:373–86.
- [29] Saraseta-Zabala E, Aguesse F, Villarreal I, Rodriguez-Martinez LM, López CM, Kubik P. Understanding lithium inventory loss and sudden performance fade in cylindrical cells during cycling with deep-discharge steps. *J Phys Chem C* 2015;119(2):896–906.
- [30] Pop V, Bergveld HJ, Regtien PP, het Veld JO, Danilov D, Notten PHL. Battery aging and its influence on the electromotive force. *J Electrochem Soc* 2007;154(8):A744.
- [31] Birk C. Oxford battery degradation dataset 1. Oxford, Oxford,U.K.: Univ.; 2017.
- [32] Birk C. Diagnosis and prognosis of degradation in lithium-ion batteries. DPhil thesis, Oxford, U.K.: Univ. Oxford; 2017.
- [33] Lin M, Wu D, Meng J, Wang W, Wu J. Health prognosis for lithium-ion battery with multi-feature optimization. *Energy* 2023;264:126307.
- [34] Tian J, \*\*ong R, Shen W. State-of-health estimation based on differential temperature for lithium ion batteries. *IEEE Trans Power Electron* 2020;35(10):10363–73.
- [35] Saha B, Goebel K. “Battery data set,” NASA ames prognostics data repository. 2007 [Online]. Available: <http://ti.arc.nasa.gov/project/prognostic-data-repository>.